Nonlinear Dyn (2007) 47:405–419
DOI 10.1007/s11071-006-9039-7

ORIGINAL ARTICLE

# Global bifurcations and chaos in a harmonically excited and undamped circular plate

**S. B. Samoylenko · W. K. Lee**

Received: 13 June 2005 / Accepted: 14 February 2006 / Published online: 16 June 2006


**Abstract** Global bifurcations and chaos in modal interactions of an imperfect circular plate with one-to-one internal resonance are investigated. The case of primary resonance, in which an excitation frequency is near natural frequencies, is considered. The damping force is not included in the analysis. The method of multiple scales is used to obtain an autonomous system from a non-autonomous system of ordinary differential equations governing non-linear oscillations of an imperfect circular plate. The Melnikov's method for heteroclinic orbits of the autonomous system is used to obtain the criteria for chaotic motion. It is shown that the existence of heteroclinic orbits in the unperturbed system implies chaos arising from breaking of heteroclinic orbits under perturbation. The validity of the result is checked numerically. It is also observed numerically that chaos can appear due to breaking of invariant tori under perturbation.

**Keywords** Nonlinear vibration of circular plate · Global bifurcation · Melnikov's method

S. B. Samoylenko · W. K. Lee (✉)
Institute of Volcanology and Seismology, 9, Piip Ave., Pertopavlovsk-Kamchatsky, 683006, Russia
e-mail: samsergey@kscnet.ru
School of Mechanical Engineering, Yeungnam University, Gyongsan, 712-749 Republic of Korea
e-mail: wklee@yu.ac.kr

## 1. Introduction

Plates having two of their linear natural frequencies nearly equal exhibit complicated and interesting phenomena when nonlinear terms are taken into account.

Amongst the first theoretical analyses on the nonlinear vibration of circular disks were those by Tobias [1], where the non-linear, undamped vibration of imperfect circular disks was studied, and Williams and Tobias [2] where the undamped non-linear vibration of imperfect disk subject to space-fixed harmonic excitation was analyzed.

For local bifurcations, modal interactions of rectangular plates with one-to-one internal resonance have been studied by many researchers. Sridhar et al. [3] and Hadian and Nayfeh [4] studied symmetric responses in primary resonance of a circular plate with three-mode interaction. Lee and Kim [5] studied combination resonances of the plate. Sridhar et al. [6] derived solvability conditions for asymmetric responses in four-mode interaction of a circular plate. Nayfeh and Vakakis [7] found subharmonic traveling waves in a circular plate. Yeo and Lee [8] found that Sridhar et al.'s solvability conditions were misderived, and corrected the conditions. They observed that in the primary resonance, the steady-state response can have not only the form of standing wave but also the form of traveling wave. Using the corrected solvability conditions, Lee and Yeo [9] investigated modal interactions of a circular plate on an elastic foundation with one-to-three internal resonance. Lee et al. [10] studied the effect of

the number of nodal diameters on the interactions of the plate. Touzé, Thomas and Chaigne [11, 12] presented detailed theoretical and experimental study of asymmetric vibrations of an imperfect circular plate with one-to-one internal resonance.

Global bifurcations leading to dramatic changes in the system behavior have been examined for a wide class of problems. Feng and Sethna [13] studied global bifurcations of a Hamiltonian system with a certain symmetry in terms of breaking of homoclinic and heteroclinic orbits. Kovačič and Wiggins [14] used Melnikov's method to obtain a sufficient condition for the existence of Silnikov type homoclinic orbits in the non-linear Schrödinger equation. Raman and Mote [15] studied period-doubling, Rössler-type chaotic attractor and boundary crises phenomena in motion of an imperfect spinning plate. Yeo and Lee [16] studied global bifurcations in modal interactions of a circular plate using Wiggins and Kovačič method. Having found a sufficient condition under which Silnikov type homoclinic orbit can exist, they failed to observe any numerical evidences of global bifurcation.

In this study we extended Yeo and Lee's work [16] to investigate heteroclinic orbits created in a non-resonance case. In order to simplify the problem we consider the undamped system. Melnikov method [17, 18] was used to study global bifurcations due to breaking of homoclinic orbits.

## 2. Governing equations

The equations governing the free, undamped oscillations of non-uniform circular plates were derived by Efstathiades [19]. Yeo and Lee [16] simplified these Equations to fit the special case of non-uniform circular plate shown in Fig. 1, for which forcing terms were added. They assumed that transverse displacement of the plate could be expressed as a combination of two linearized modes. Neglecting damping terms we reduce the system as follows:

$$\ddot{x}_j + \omega_j^2 x_j + \varepsilon\gamma\omega_j^2 x_j\left(x_1^2 + x_2^2\right) = \varepsilon\mu_j \cos\lambda t, \quad j = 1, 2, \tag{1}$$

where $x_j$ are amplitudes of normal modes, $\omega_j$ are normal frequencies, $\gamma$ plays a role of the parameter of non-linearity, $\mu_j$ are amplitudes of excitation and $\varepsilon$ is a small parameter. Equations (1) were derived from

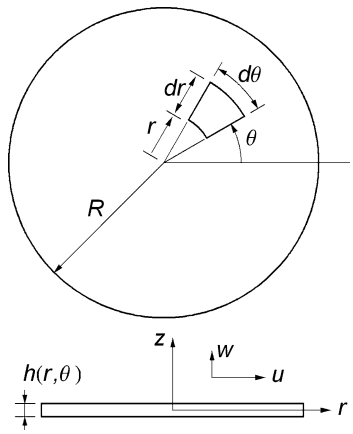


**Fig. 1** A schematic diagram of a circular plate

partial differential equations without using any specified boundary conditions [16]. Boundary conditions determine values of normal frequencies $\omega_1$, $\omega_2$ and nonlinear parameter $\gamma$, but does not affect the form of Equations (1).

The difference between system (1) and one studied by Yeo and Lee [16] is the scale of excitation amplitude. In their work for a subharmonic resonance they assumed the excitation amplitude to be order of 1. In this study, however, the amplitude is assumed to be order of $\varepsilon$ to have the same order of magnitude as nonlinear terms.

In order to consider internal resonance due to imperfection, $\omega_1 \approx \omega_2$, and external resonance due to forcing, $\lambda \approx \omega_1$, we introduce two parameters $\beta$ and $\sigma$ as follows:

$$\omega_2 = \omega_1 + \varepsilon\beta, \quad \omega_1 = \lambda + \varepsilon\sigma, \tag{2}$$

where $\beta$ and $\sigma$ are called internal and external detuning parameters, respectively. Substituting Equation (2) into system (1) and neglecting terms order of $\varepsilon^2$, we have

$$\ddot{x}_1 + (\lambda^2 + 2\varepsilon\lambda\sigma)x_1 + \varepsilon\gamma\lambda^2 x_1\left(x_1^2 + x_2^2\right) = \varepsilon\mu_1 \cos\lambda t, \tag{3a}$$

$$\ddot{x}_2 + [\lambda^2 + 2\varepsilon\lambda(\sigma + \beta)]x_2 + \varepsilon\gamma\lambda^2 x_2\left(x_1^2 + x_2^2\right) = \varepsilon\mu_2 \cos\lambda t. \tag{3b}$$

In order to use the method of multiple scales [20] we assume

$$x_j(t) = x_{j0}(T_0, T_1, \ldots) + \varepsilon x_{j1}(T_0, T_1, \ldots), \quad j = 1, 2, \tag{4}$$

where $T_k = \varepsilon^k t, \quad k = 0, 1, \ldots$. Substituting Equation (4) into Equation (3) and equating coefficients of like powers of $\varepsilon$ yield

$O(1)$:

$$D_0 x_{j0} + \lambda^2 x_{j0} = 0, \quad j = 1, 2 \tag{5}$$

$O(\varepsilon)$:

$$\begin{aligned} D_0^2 x_{11} + \lambda^2 x_{11} = & -2D_0 D_1 x_{10} - 2\lambda\sigma x_{10} \\ & -\gamma\lambda^2\left(x_{10}^3 + x_{10}x_{20}^2\right) \\ & +\mu_1 \cos\lambda T_0 \end{aligned} \tag{6a}$$

$$\begin{aligned} D_0^2 x_{21} + \lambda^2 x_{21} = & -2D_0 D_1 x_{20} - 2\lambda(\sigma+\beta) x_{20} \\ & -\gamma\lambda^2\left(x_{20}^3 + x_{20}x_{10}^2\right) \\ & +\mu_2 \cos\lambda T_0. \end{aligned} \tag{6b}$$

The general solution of Equation (5) can be written in the form

$$x_{j0} = Z_j(T_1)e^{i\lambda T_0} + Z_j^*(T_1)e^{-i\lambda T_0}, \tag{7}$$

where $i = \sqrt{-1}$ and asterisk denotes complex conjugate. The functions $Z_j(T_1)$ are to be determined by satisfying the solvability conditions for boundedness of the solution. Substituting Equation (7) into (6) we obtain solvability conditions as follows:

$$\begin{aligned} Z_1' = i\Bigg[ & \varepsilon F_1 + \sigma Z_1 + \frac{3}{2}\gamma\lambda Z_1^2 Z_1^* + \gamma\lambda Z_1 Z_2 Z_2^* \\ & + \frac{1}{2}\gamma\lambda Z_2^2 Z_1^* \Bigg] \end{aligned} \tag{8a}$$

$$\begin{aligned} Z_2' = i\Bigg[ & \varepsilon F_2 + (\sigma+\beta) Z_2 + \frac{3}{2}\gamma\lambda Z_2^2 Z_2^* \\ & + \gamma\lambda Z_2 Z_1 Z_1^* + \frac{1}{2}\gamma\lambda Z_1^2 Z_2^* \Bigg], \end{aligned} \tag{8b}$$

where

$$F_j = -\frac{\mu_j}{4\varepsilon\lambda}$$

and a prime denotes differentiation with respect to slow time $T_1$.

Assuming harmonic amplitudes $Z_j(T_1)$ as follows:

$$Z_j(T_1) = \sqrt{2a_j}(\sin\phi_j + i\ \cos\phi_j)$$

and introducing new variables:

$$\begin{aligned} & p_1 = a_1, \quad q_1 = \phi_1 - \phi_2, \\ & p_2 - p_1 = a_2, \quad q_2 = \phi_2, \end{aligned} \tag{9}$$

we transform system (8) to the following form

$$\begin{aligned} p_1' = & 2\gamma\lambda p_1(p_1 - p_2)\sin 2q_1 \\ & + \varepsilon F_1\sqrt{2p_1}\cos(q_1 + q_2) \\ q_1' = & \beta + \gamma\lambda(-1 + \cos 2q_1)(2p_1 - p_2) \\ & + \left[\frac{F_2}{\sqrt{2(p_2 - p_1)}}\sin\ q_2 - \frac{F_1}{\sqrt{2p_1}}\sin(q_1 + q_2)\right] \\ p_2' = & \varepsilon\Bigg[F_1\sqrt{2p_1}\cos(q_1 + q_2) \\ & + F_2\sqrt{2(p_2 - p_1)}\cos\ q_2\Bigg] \\ q_2' = & -\beta - \sigma + \gamma\lambda(-1 + \cos 2q_1)p_1 \\ & - 3\gamma\lambda p_2 - \varepsilon\frac{F_2}{\sqrt{2(p_2 - p_1)}}\sin\ q_2. \end{aligned}$$

Rescaling variables

$$\begin{aligned} & p_j = \frac{P_j}{\gamma\lambda}, \qquad q_j = \frac{\pi}{2} + Q_j, \\ & F_1 = -\frac{f_1}{\sqrt{\gamma\lambda}}, \quad F_2 = \frac{f_2}{\sqrt{\gamma\lambda}} \end{aligned} \tag{10}$$

allows to rewrite this system in a simpler way:

$$\begin{aligned} P_1' = & 2P_1(P_2 - P_1)\sin 2Q_1 \\ & + \varepsilon f_1\sqrt{2P_1}\cos(Q_1 + Q_2) \end{aligned} \tag{11a}$$

$$\begin{aligned} Q_1' = & \beta - (1 + \cos 2Q_1)(2P_1 - P_2) \\ & + \varepsilon\left[\frac{f_2}{\sqrt{2(P_2 - P_1)}}\cos Q_2\right. \\ & \left. - \frac{f_1}{\sqrt{2P_1}}\sin(Q_1 + Q_2)\right] \end{aligned} \tag{11b}$$

$$\begin{aligned} P_2' = & \varepsilon\Bigg[f_1\sqrt{2P_1}\cos(Q_1 + Q_2) \\ & - f_2\sqrt{2(P_2 - P_1)}\sin\ Q_2\Bigg] \end{aligned} \tag{11c}$$

$$Q_2' = -\beta - \sigma + (1 + \cos 2Q_1)\, P_1 - 3P_2 - \varepsilon \frac{f_2}{\sqrt{2\,(P_2 - P_1)}} \cos\, Q_2. \tag{11d}$$

Since this is a Hamiltonian system, we can express the system as follows:

$$\dot{P}_1 = -\frac{\partial H}{\partial Q_1}, \quad \dot{Q}_1 = \frac{\partial H}{\partial P_1},$$
$$\dot{P}_2 = -\frac{\partial H}{\partial Q_2}, \quad \dot{Q}_2 = \frac{\partial H}{\partial P_2}$$

with Hamiltonian

$$H = H_0 + \varepsilon H_1,$$
$$H_0 = \beta P_1 - (\beta + \sigma) P_2 - (1 + \cos 2Q_1) \times P_1 (P_1 - P_2) - \frac{3}{2} P_2^2,$$
$$H_1 = -f_1 \sqrt{2P_1} \sin(Q_1 + Q_2) - f_2 \sqrt{2\,(P_2 - P_1)} \cos Q_2.$$

According to Equations (9) $P_1$ and $P_2$ represent the amplitude of the mode $x_1$ and the total of two modes $x_1 + x_2$, respectively. Therefore $P_1$ satisfies condition

$$0 \le P_1 \le P_2. \tag{12}$$

This condition implies that function $H$ has only real values.

## 3. Unperturbed system

Let us consider an unperturbed system, which corresponds to case $\varepsilon = 0$ in system (11) as follows:

$$P_1' = 2P_1\,(P_2 - P_1) \sin 2Q_1 \tag{13a}$$
$$Q_1' = \beta - (1 + \cos 2Q_1)(2P_1 - P_2) \tag{13b}$$
$$P_2' = 0 \tag{13c}$$
$$Q_2' = -\beta - \sigma + (1 + \cos 2Q_1)\, P_1 - 3P_2. \tag{13d}$$

System (13) is a completely integrable Hamiltonian system with $P_2 = P_{20}$ as a conserved quantity.

In view of the structure of system (13) study of the flow in two-dimensional space $(P_1, Q_1)$ may be useful to understand the system. Thus we study fixed points and orbits of corresponding system

$$P_1' = 2P_1\,(P_{20} - P_1) \sin 2Q_1 \tag{14a}$$
$$Q_1' = \beta - (1 + \cos 2Q_1)\,(2P_1 - P_{20}). \tag{14b}$$

It has five fixed points, whose locations depend on two parameters $\beta$ and $P_{20}$:

$$P_1 = \frac{1}{4}\,(\beta + 2P_{20}), \quad Q_1 = \pi n \tag{15a}$$
$$P_1 = 0, \qquad Q_1 = 2\pi n \pm \tilde{Q}_1 \tag{15b}$$
$$P_1 = P_{20}, \quad Q_1 = 2\pi n \pm \tilde{Q}_1, \tag{15c}$$

where

$$\tilde{Q}_1 = \arccos\left[\sqrt{\frac{|\beta|}{2P_{20}}}\right]$$

and $n = 0, 1, 2, \ldots$. Analysis of stability of system (14) shows that point (15a) is center and points (15b,c) are saddle points. At the fixed points, in view of Equation (13d), $Q_2'$ is a constant, which implies the rotation of the flow considering that $Q_2$ is an angle variable. Therefore fixed points in two-dimensional system (14) correspond to invariant tori in four-dimensional system (13).

Returning to coordinates $(a_1, a_2, \phi_1, \phi_2)$ gives us physical meaning of these solutions in terms of plate oscillations. Let's consider the possibility of existence of a periodic solution of system (1), with (i) $x_1 = 0$ or $x_2 = 0$, or (ii) $x_1 \neq 0$ and $x_2 \neq 0$. The former is called a single-mode solution and the later a mixed-mode solution. There may exist two types of single-mode solutions. One is $x_1$-mode ($x_2 = 0$) and the other $x_2$-mode ($x_1 = 0$). In view of (9) and (10) coordinates $P_1$ and $P_2 - P_1$, respectively, denote the amplitudes of $x_1$ and $x_2$. In other words, $P_2$ denotes the sum of both amplitudes. Therefore, vanishing of $P_1$ means single-mode ($x_1$-mode) solution, while non-vanishing of $P_1$ does mixed-mode ($x_1$- and $x_2$- mode) solution. Another single mode ($x_1$-mode) solution exists when $P_2 - P_1 = 0$. Since center (15a) has non-vanishing $P_1$ and $P_2 - P_1$, it turns out to be a mixed-mode solution. Saddle-point (15b) has vanishing $P_1$, while saddle-point (15c) has vanishing $P_2 - P_1$. Therefore, saddle-points (15b) and

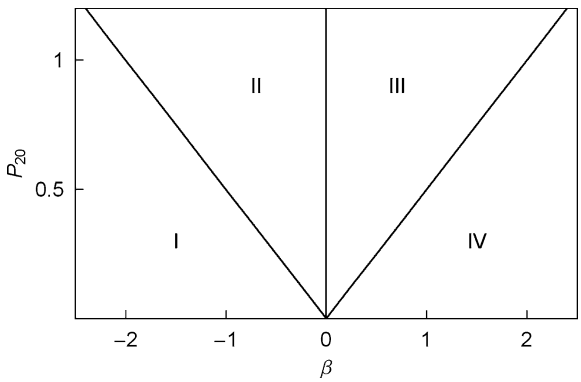


**Fig. 2** Global bifurcation diagram of unperturbed system (14).

(15c) turn out to be single-mode solutions, $x_2$-mode and $x_1$-mode, respectively.

For the system (14) it is possible to study global bifurcations in the $(\beta, P_{20})$ parameter plane shown in Fig. 2, where exist four regions

$$\text{(I)} \quad \beta < -2P_{20}, \qquad \text{(II)} \quad -2P_{20} < \beta < 0,$$
$$\text{(III)} \quad 0 < \beta < 2P_{20}, \quad \text{(IV)} \qquad 2P_{20} < \beta.$$

Each of these has qualitatively different behavior of the flow as shown in Fig. 3. For regions I and IV there are neither homoclinic nor heteroclinic orbits in $(Q_1, P_1)$-plane considering condition (12). For regions II and III each phase portrait contains three heteroclinic orbits $(A,\ A',\ A''$ in II and $B,\ B',\ B''$ in III). We will consider breaking of heteroclinic orbits under perturbation and consequences of this breaking. Therefore regions II and III will be of our interest.

Yang and Sethna [21] have studied global bifurcation of a nearly square plate. The system (11) could be considered as a particular case of system (5.3) in [21] for which parameter $K = -1$. The global bifurcation analysis given in [21] considers as a bifurcation parameter quantity proportional to $\frac{\beta}{P_{20}}$ and excludes case $K = -1$ because of singularity. In present work we adapt parameters $\beta$ and $P_{20}$ to avoid the singularity and study the global bifurcations of case $K = -1$.

## 4. Perturbed system and Melnikov theory

In order to investigate the behavior of the perturbed system (11) we use generalized multidimensional Melnikov's method [18]. Let's consider a system having some invariant sets (fixed points or invariant manifolds, such as invariant tori), whose stable manifolds tangentially intersect unstable manifolds to construct

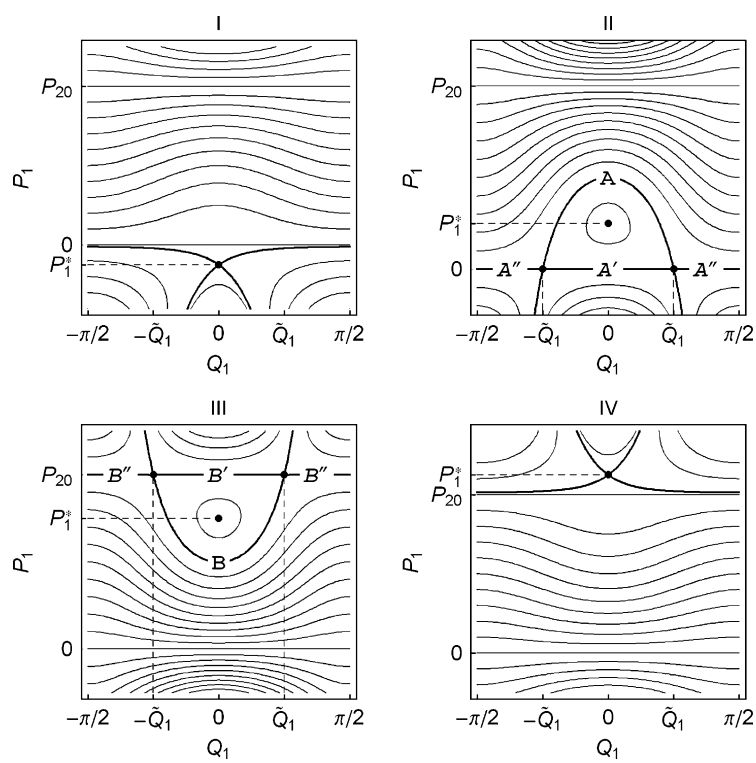


**Fig. 3** Phase portraits of system (14) in different regions on bifurcation diagram Figure 2. Here $P_1^* = (\beta + 2P_{20})/4$.

homoclinic or heteroclinic orbits. When the system is exposed to a small perturbation, stable and unstable manifolds of these invariant sets may no longer construct homoclinic or heteroclinic orbits, which means that stable and unstable manifolds split up. However, as shown in [17, 18] stable manifolds may transversally intersect unstable manifolds, in this case intersection points compose countably infinite set having complicated Cantor-set type. This phenomenon leads to chaos through generation of Smale's horseshoes [22, 23].

The main goal of Melnikov's method is to estimate the minimal distance between splitted manifolds of hyperbolic invariant manifold and find the conditions under which this distance vanishes. The leading term of this distance could be expressed as a certain function of system parameters called "Melnikov function", therefore transversal crossing of splitted manifolds occurs when Melnikov function has simple zero. The Melnikov function could be expressed by an improper integral. We will use expressions for Melnikov function derived in [18]. In our case of four-dimensional completely integrable system Melnikov integral has form:

$$\begin{aligned} M &= \lim_{l\to\infty}\int_{-T_l^u}^{T_l^s}\frac{\partial H_1}{\partial Q_2}dt \\ &= -\sqrt{2}\lim_{l\to\infty}\int_{-T_l^u}^{T_l^s}[f_1\sqrt{P_1}\cos(Q_1+Q_2) \\ &\quad -f_2\sqrt{P_2-P_1}\sin Q_2]dt, \end{aligned} \tag{16}$$

where limits $T_l^s$ and $T_l^u$ are sequences of time, which go to infinity as index $l$ does.

Calculation of the integral (16) requires evaluation of integrands along unperturbed heteroclinic orbits, and therefore knowledge of the explicit dependence of variables $P_1$, $Q_1$ and $Q_2$ on time. In other words we have to build up a parametrization of this orbits. Equations that give time parametrization of heteroclinic orbits are given in Appendix A.

### 4.1. Calculation of Melnikov function

It is possible to simplify integral (16) noting that the structure of explicit expressions for $Q_2$ in (A.5)–(A.21) has form

$$Q_2 = \tilde{Q}_2 + Q_{20},$$

where $\tilde{Q}_2$ is a function of time and $Q_{20}$ is an arbitrary constant. Using this representation we may transform the integrand of (16):

$$\begin{aligned} &f_1\sqrt{P_1}\cos(Q_1+Q_2) - f_2\sqrt{P_2-P_1}\sin(Q_2) \\ &= f_1\sqrt{P_1}[\cos(Q_1+\tilde{Q}_2)\cos\ Q_{20} \\ &\quad -\sin(Q_1+\tilde{Q}_2)\ \sin Q_{20}] \\ &\quad -f_2\sqrt{P_2-P_1}[\cos\tilde{Q}_2\sin\ Q_{20}-\sin\ \tilde{Q}_2\cos Q_{20}] \\ &= -\cos\ Q_{20}[f_1\sqrt{P_1}\cos(Q_1+\tilde{Q}_2) \\ &\quad +f_2\sqrt{P_2-P_1}\sin\tilde{Q}_2] \\ &\quad +\sin Q_{20}[f_1\sqrt{P_1}\sin(Q_1+\tilde{Q}_2) \\ &\quad +f_2\sqrt{P_2-P_1}\cos\ \tilde{Q}_2]. \end{aligned}$$

So integral (16) could be expressed as:

$$\begin{aligned} M &= -\sqrt{2}\cos Q_{20}(f_1I_1+f_2I_2) \\ &\quad +\sqrt{2}\sin Q_{20}(f_1I_3+f_2I_4), \end{aligned} \tag{17}$$

where

$$I_1 = \lim_{l\to\infty}\int_{-T_l^u}^{T_l^s}\sqrt{P_1}\cos(Q_1+\tilde{Q}_2)\,dt$$

$$I_2 = \lim_{l\to\infty}\int_{-T_l^u}^{T_l^s}\sqrt{P_2-P_1}\sin\tilde{Q}_2\,dt$$

$$I_3 = \lim_{l\to\infty}\int_{-T_l^u}^{T_l^s}\sqrt{P_1}\sin(Q_1+\tilde{Q}_2)\,dt$$

$$I_4 = \lim_{l\to\infty}\int_{-T_l^u}^{T_l^s}\sqrt{P_2-P_1}\cos\tilde{Q}_2\ dt.$$

Substitution of explicit time dependencies (A.2)∼(A.5) to Equation (17) and computation of integrals give for the heteroclinic orbit $A$:

$$\begin{aligned} I_1 &= -\frac{\sqrt{P_{20}}\sin\tilde{Q}_1}{2e_A}\Psi_1, \\ I_2 &= I_3 = 0, \\ I_4 &= -\frac{\sqrt{P_{20}}\sin\tilde{Q}_1}{2e_A}\Psi_2. \end{aligned}$$

See Appendix B for details. Here

$$\begin{aligned} \Psi_1 = i\Bigg[&\psi\left(\frac{1}{4}-i\,\nu_A\right)-\psi\left(\frac{1}{4}+i\,\nu_A\right) \\ &+\psi\left(\frac{3}{4}+i\,\nu_A\right)-\psi\left(\frac{3}{4}-i\,\nu_A\right)\Bigg], \end{aligned}$$

$$\Psi_2 = \psi\left(\frac{1}{2} + i\,\nu_A\right) + \psi\left(\frac{1}{2} - i\,\nu_A\right) - \psi(i\,\nu_A) - \psi(-i\,\nu_A)$$

$$\nu_A = \frac{\omega_R}{4e_A} \tag{18}$$

and function $\psi(x)$ is given as

$$\psi\,(x) = \Gamma'(x)/\,\Gamma(x),$$

where $\Gamma(x)$ is the gamma function. We should note that quantities $\Psi_1$ and $\Psi_2$ are real-valued. Quantities $e_A$ and $\omega_R$ are given in (A.3) and (A.6) in Appendix A.

Now returning to (17) we may write the expression for the Melnikov function as follows:

$$M^A = \frac{\sqrt{2P_{20}}\sin\tilde{Q}_1}{2e_A}\,[f_1\Psi_1\,\cos Q_{20} - f_2\Psi_2\,\sin Q_{20}]$$

or, equivalently

$$M^A = \frac{\sqrt{2P_{20}}\,\sin\tilde{Q}_1}{2e_A} m^A(f_1,\,f_2,\,\nu_A) \times \cos\,[Q_{20} - \phi^A(f_1,\,f_2,\,\nu_A)], \tag{19}$$

where

$$m^A(f_1,\,f_2,\,\nu_A) = \sqrt{f_1\Psi_1^2 + f_2\Psi_2^2},$$

$$\phi^A(f_1,\,f_2,\,\nu_A) = \tan\left(\frac{f_1\Psi_1}{f_2\Psi_2}\right)$$

For heteroclinic orbits $A'$ and $A''$ we have

$$I_1 = I_2 = I_3 = I_4 = 0.$$

Therefore we have the Melnikov functions for these orbits:

$$M^{A'} = M^{A''} = 0. \tag{20}$$

By use of explicit time dependencies (A.13)$\sim$(A.15) Equation (17) gives for the heteroclinic orbit $B$:

$$I_1 = \frac{\pi\sqrt{P_{20}}\sin\tilde{Q}_1}{e_A}\left\{\frac{1}{\sinh\nu_B} - \frac{1}{\nu_B}\right\},$$

$$I_2 = I_3 = 0,$$

$$I_4 = \frac{\pi\sqrt{P_{20}}\sin\tilde{Q}_1}{e_A\cosh\nu_B},$$

where

$$\nu_B = \frac{\pi(\beta - \omega_R)}{2e_A} \tag{21}$$

The Melnikov function for orbit $B$ becomes

$$M^B = -\frac{\pi\sqrt{P_{20}}\sin\tilde{Q}_1}{e_A}\left[f_1\left\{\frac{1}{\sinh\nu_B} - \frac{1}{\nu_B}\right\} \times\cos Q_{20} - \frac{f_2}{\cosh\nu_B}\sin Q_{20}\right],$$

or equivalently

$$M^B = -\frac{\pi\sqrt{P_{20}}\sin\tilde{Q}_1}{e_A} m^B\,(f_1,\,f_2,\,\nu_B) \times\cos[Q_{20} - \phi^B(f_1,\,f_2,\,\nu_B)], \tag{22}$$

where

$$m^B(f_1,\,f_2,\,\nu_B) = \sqrt{f_1^2\left(\frac{1}{\sinh\nu_B} - \frac{1}{\nu_B}\right)^2 + \frac{f_2^2}{\cosh^2\nu_B}},$$

$$\phi^B\,(f_1,\,f_2,\,\nu_B) = \tan\left[\frac{f_1}{f_2}\left(\coth\nu_B - \frac{\cosh\nu_B}{\nu_B}\right)\right],$$

For orbits $B'$ and $B''$ we have

$$M^{B'} = M^{B''} = 0. \tag{23}$$

Finally, gathering Equations (18), (21), (22) and (23) we have Melnikov functions for all orbits as follows:

$$M^{A,B} \propto m^{A,B}\cos(Q_{20} + \phi^{A,B}) \tag{24}$$

and

$$M^{A'} = M^{A''} = M^{B'} = M^{B''} = 0. \tag{25}$$

According to the Melnikov theory [17, 18] transversal intersections of stable and unstable invariant manifolds appear when the Melnikov function, a function of parameters, has simple zeros. Moreover, we need to prove the existence of simple zeros, but we don't need to determine their locations in parameter space.

For heteroclinic orbits $A$ and $B$ Melnikov function given by Equations (19) and (22) depends on the parameter $Q_{20}$ (special value of a phase variable $Q_2$) and system parameters $\beta, \sigma, P_{20}, f_1, f_2$. The parameter $Q_{20}$ appears in integration and determines the starting point in time parametrization of heteroclinic orbits in the unperturbed system. We see that even when all system parameters are fixed, Melnikov function being a function of $Q_{20}$ definitely has simple zeros. It means that when unperturbed system has heteroclinic orbits $A$ and $B$, under perturbation this orbits can break and transversal intersections of invariant manifolds can take place, except for some cases to be discussed later. In other words, chaos led by breaking of heteroclinic orbits occurs everywhere in regions II (orbit $A$) and III (orbit $B$) of Fig. 2.

It is necessary to pay some attention to simplicity of zeros. In order to study the cases in which Melnikov function having form (24) is identically zero, we need to find conditions for $m^{A,B} = 0$. Consider first $M^A$. Since both $\Psi_1$ and $\Psi_2$ are real, $m^A$ is strictly positive and equal to zero only when $f_1\Psi_1 = f_2\Psi_2 = 0$. Quantities $\Psi_1$ and $\Psi_2$ vanish only when $\nu_A = 0$. According to Equation (18) it implies

$$\omega_R = \beta + \sigma + 3P_{20} = 0.$$

Referring to [14], we call this a resonance. In the resonance $Q_2$ in unperturbed case is constant on the invariant manifolds. Moreover, $m^A$ is equal to zero if $f_1 = f_2 = 0$ meaning no excitation. Consider $M^B$ next. Function $m^B$ is equal to zero when $\nu_B = 0$. According to Equation (21) it implies a resonance condition

$$\beta - \omega_R = \sigma + 3P_{20} = 0.$$

It is obvious to see that $m^B$ is equal to zero when $f_1 = f_2 = 0$. In cases of resonance and no excitation, Melnikov functions $M^A$ and $M^B$ being identical zero imply that the distance between stable and unstable manifolds of hyperbolic tori is equal to zero everywhere. This means that the perturbation does not break the heteroclinic orbits. In resonance, however, absence of breaking of heteroclinic orbits under perturbation does not imply the absence of chaos [14]. The nature of chaos due to resonance is different from the one of chaos due to breaking of heteroclinic orbits. In resonance homoclinic orbit of Silnikov type can occur and hence Silnikov chaos can take place [14, 22].

For heteroclinic orbits $A'$, $A''$, $B'$ and $B''$, the identical zero of Melnikov function in Equation (25) does not tell whether those orbits break under perturbation or not. Pairs of orbits $A'$, $A''$ and $B'$, $B''$ correspond to lines $P_1 = 0$ and $P_1 = P_{20}$, respectively. In contrast to the unperturbed system (13) the perturbed system (11) does not have solutions on these lines, in view of Equation (12). For the perturbed system these lines bound the domain in which solutions exist.

## 5. Numerical examples

The coordinates $P_1$, $Q_1$, $P_2$, $Q_2$ belong in $\mathbb{R}^1 \times S^1 \times \mathbb{R}^1 \times S^1$, where $S^1$ is a circle of length $2\pi$. Thus we have a two-torus in four-dimensional space. Unperturbed system (13) shows that coordinates $P_1$, $Q_1$ and $P_2$ do not depend on $Q_2$. Therefore, in order to understand flows in four-dimensional space we can use a projection of phase portraits on a three-dimensional space $(P_1, Q_1, P_2)$.

To illustrate the behavior of stable and unstable manifolds of invariant tori for perturbed system (11) we set up the Poincaré section given by

$$\Sigma_{Q_2} = \{Q_2 = 0, \dot{Q}_2 > 0\}$$

and build a three-dimensional Poincaré map [22, 23]. It should be noted that system (11) is Hamiltonian and all solutions lie on a manifold $H = constant$. The intersection of Poincaré map and this manifold is a two-dimensional smooth surface. The hyperbolic invariant tori of flow (11) with stable and unstable invariant manifolds correspond to hyperbolic fixed points of the Poincaré map with one-dimensional stable and unstable invariant manifolds. Two-dimensional projections of the Poincaré map for cases II and III in Fig. 3 are shown in Figs. 4 and 5, respectively. Solid and dotted lines, respectively, denote stable and unstable manifolds of fixed points. We can see the typical pattern of heteroclinic tangles [17, 22] appearing when manifolds intersect transversely. These illustrations verify that under perturbation heteroclinic orbits $A$ and $B$ are broken with subsequent intersection of stable and unstable invariant manifolds. Lines $P_1 = 0$ and $P_1 = P_{20}$ which correspond to these orbits and bound the domain

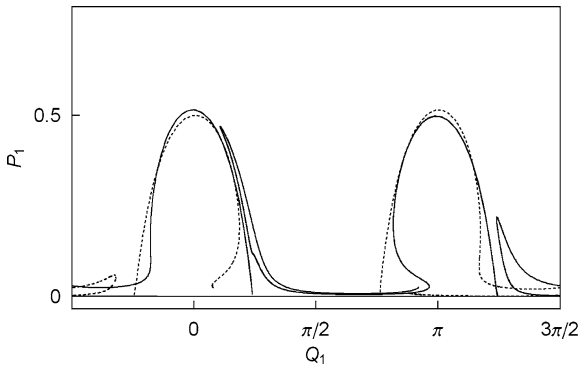


**Fig. 4** Intersection of stable and unstable manifolds of hyperbolic fixed point on the Poincaré section in $(P_1,\ Q_1)$-plane for case II of Fig. 3, for $\varepsilon = 0.05,\ f_1 = 0.5,\ f_2 = 1.0,\ \sigma = -0.25,\ \beta = -1.1,\ P_{20} = 1.0$

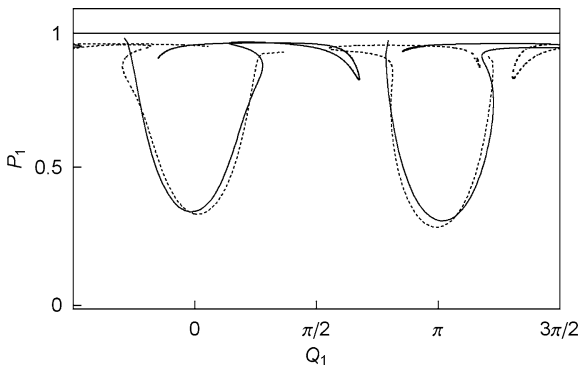


**Fig. 5** Intersection of stable and unstable manifolds of hyperbolic fixed point on the Poincaré section in $(P_1,\ Q_1)$-plane for case II of Fig. 3 for $\varepsilon = 0.05,\ f_1 = 1.0,\ f_2 = 3.0,\ \sigma = -0.25,\ \beta = 1.0,\ P_{20} = 1.0$

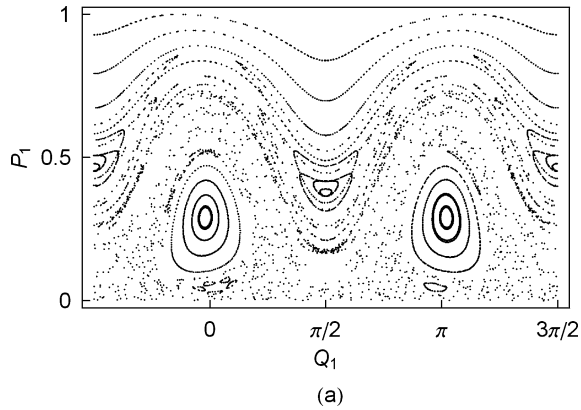


**Fig. 6** Poincaré sections of flow (11) for a number of different starting points in $(P_1,\ Q_1)$-plane for case II on Fig. 3 for $(\varepsilon = 0.05,\ f_1 = 0.5,\ f_2 = 1.0,\ \sigma = -0.25,\ \beta = -1.1,\ P_{20} = 1.0)$

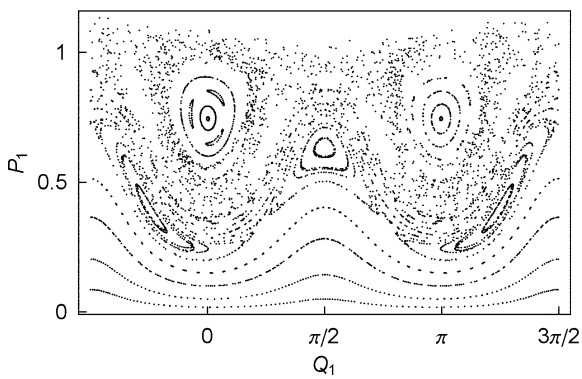


**Fig. 7** Poincaré sections of flow (11) for a number of different starting points in $(P_1,\ Q_1)$-plane for case III on Fig. 3 for $(\varepsilon = 0.05,\ f_1 = 0.5,\ f_2 = 1.0,\ \sigma = -0.25,\ \beta = 1.0,\ P_{20} = 1.0)$

where system's solutions exist are shown, respectively, in Figs. 4 and 5.

Heteroclinic intersections of stable and unstable manifolds imply the presence of horseshoe type dynamics and hence chaos. Building a sequence of Poincaré maps for different starting points could approve chaotic behavior. In order to verify the validity of the results by Melnikov method, we obtained Poincaré maps built for cases II and III in Fig. 3 shown in Figs. 6 and 7, respectively. The pattern of maps is typical for Hamiltonian systems. Here we can see that in a neighborhood of broken heteroclinic orbits Poincaré maps form stochastic layers. We believe that this pattern verifies the validity of the results by Melnikov method as expected in the previous section. We can observe some overlappings of trajectories in Fig. 6. It appears because Fig. 6 represents two-dimensional projection of three-dimensional Poincaré sections.

For both cases II and III in Figs. 6 and 7 the Poincaré maps around the centers are similar with the phase portraits around the center in Fig. 3 (II) and (III), respectively. Therefore, mixed mode solutions $(0 < P_1 < P_2)$, corresponding to center (15a), and solutions close to it do not change qualitatively under perturbation. However, perturbed system has no single-mode solutions ($x_2$-mode and $x_1$-mode for case II and III, respectively). The vicinity of unperturbed single-mode solutions and heteroclinic orbits on the Poincaré map is filled by stochastic layer, which corresponds to chaotic mixed-mode motion.

We want to look closely how Poincaré map changes as parameter values cross the boundary between regions III and IV, respectively, expected as chaotic and

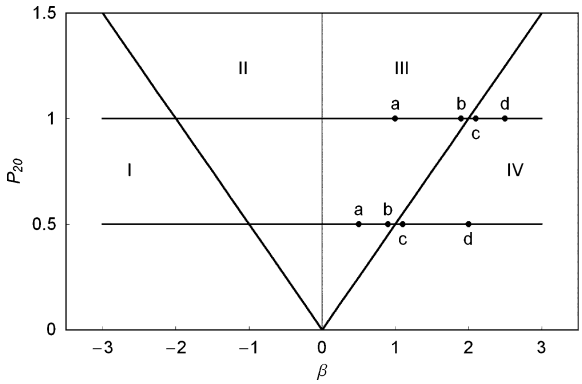


**Fig. 8** Poincaré sections of flow (11) for a number of different starting points in $(P_1, Q_1)$-plane for case III on Fig. 3 for ($\varepsilon = 0.05,\ f_1 = 0.5,\ f_2 = 1.0,\ \sigma = -0.25$).

non-chaotic regions. For this purpose four points with coordinates $P_{20} = 1$ and $\beta = 1.0, 1.9, 2.1, 2.5$ were chosen on the bifurcation diagram as shown in Fig. 8. Poincaré sections corresponding to these points are shown in Fig. 9(a–d), respectively. For $P_{20} = 1$ boundary between regions III and IV corresponds to $\beta = 2$. It is shown in Fig. 9(a) and (b) that as internal detuning parameter $\beta$ approaches 2, heteroclinic orbit $B$ shrinks and so does the chaotic layer caused by breaking of this orbit. Finally for $\beta > 2.0$ orbit $B$ disappears and Poincaré section doesn't have wide chaotic layers as shown in Fig. 9(c) and (d). This verifies that the boundary between regions III and IV separates chaotic and non-chaotic regions as expected. Fig. 10 presents a sequence of Poincaré sections for points with coordinates $P_{20} = 0.5$ and $\beta = 0.5, 0.9, 1.1$ and 2.0, shown in Fig. 8. In this case $\beta = 1$ is on the boundary between regions III and IV. We see that Poincaré sections for $\beta > 1$ have wide stochastic layers. Contrast to Fig. 9, Fig. 10 shows that the boundary between regions III and IV doesn't really divide chaotic and non-chaotic regions. Chaos can appear in region IV, even though unperturbed system has no heteroclinic orbits in this region. The scenario of chaotic phenomenon shown in Fig. 10 is different from one shown in Fig. 9. For the case of Fig. 10 heteroclinic orbits, according to Poincaré-Birkhoff theorem [23], arise from resonant invariant tori due to perturbation. Breaking of these orbits leads to chaos [24, 25]. Figure 10(a) and (b) show that for values of $\beta = 0.5$ and 0.9 corresponding to region III, breaking of unperturbed heteroclinic orbits as well as orbits due to invariant tori occurs. It was observed that stochastic layers similar to ones in region IV appeared in region I, which is not shown in this paper. The transition to chaos through breaking of invariant tori could be studied analytically by use of Greene method [26] or renormalization-group technique [27–29].

In order to ensure whether behavior of the system is really chaotic or not, the largest Lyapunov exponent [23] was calculated for the flow (11). In order for an Hamiltonian system to have chaotic motion the largest Lyapunov exponent must be positive. For non-chaotic motion of an Hamiltonian system the largest Lyapunov exponent becomes zero. Figure 11 shows the largest Lyapunov exponent as a function of parameter $\beta$ for $P_{20} = 1$ and $P_{20} = 0.5$. We can see that for $P_{20} = 1$ (Fig. 11(a)), positive values of the largest Lyapunov exponent correspond to $-2 < \beta$ and $\beta < 2$ as predicted by Melnikov method. Near $\beta = 0$, heteroclinic orbits

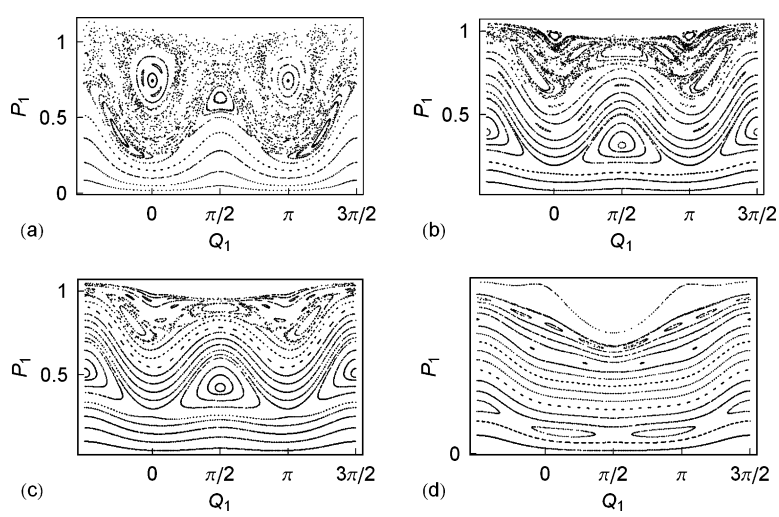


**Fig. 9** Poincaré sections of flow (12) in $(P_1, Q_1)$-plane for (a): $\beta = 1.0$, (b): $\beta = 1.9$, (c): $\beta = 2.1$, (d): $\beta = 3.0$ and $\varepsilon = 0.05$, $f_1 = 0.5,\ f_2 = 1,\ \sigma = -0.25,\ P_{20} = 1$

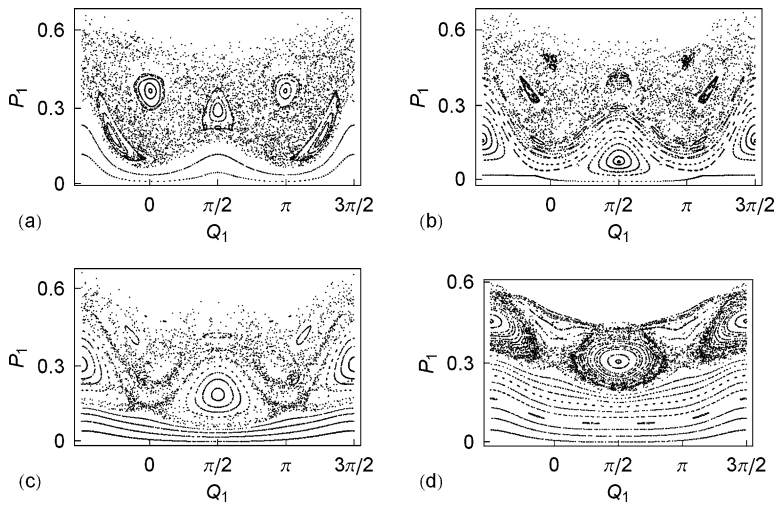


**Fig. 10** Poincaré sections of flow (12) in ($P_1$, $Q_1$)-plane for (a): $\beta = 0.5$, (b): $\beta = 0.9$, (c): $\beta = 1.1$, (d): $\beta = 2.0$ and $\varepsilon = 0.05$, $f_1 = 0.5$, $f_2 = 1$, $\sigma = -0.25$, $P_{20} = 0.5$

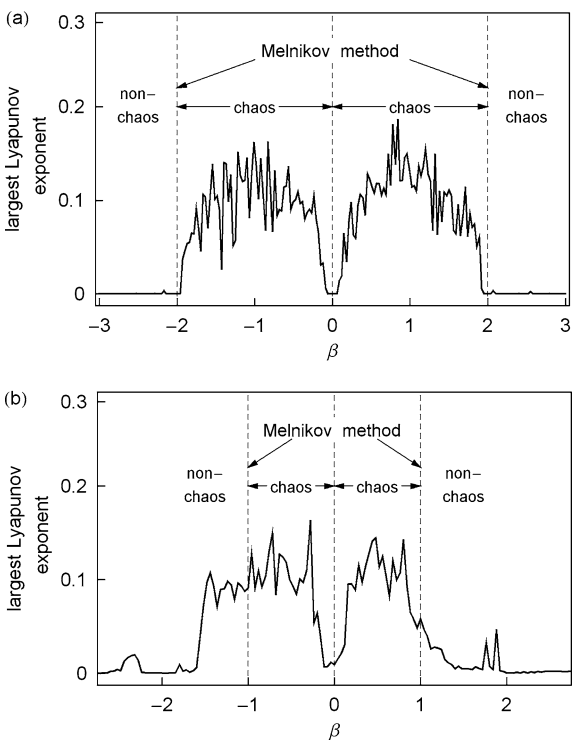


**Fig. 11** The largest Lyapunov exponent of system (11) as a function of parameter $\beta$ for $\varepsilon = 0.05$, $f_1 = 0.5$, $f_2 = 1$, $\sigma = -0.25$. 'Chaos' and 'nonchaos' denote regions predicted by Melnikov method. (a) $P_{20} = 1.0$. (b) $P_{20} = 0.5$

degenerate and therefore the largest Lyapunov exponent becomes zero. For $P_{20} = 0.5$ (Fig. 11(b)), because of breaking of the invariant tori, the chaotic region is wider than predicted. It is meaningful to compare Figs. 11 and 2, which eventually gives the boundary between chaotic and non-chaotic region predicted by Melnikov method. Further study of the transition to chaos via breaking of invariant tori is needed.

## 6. Conclusion

Global bifurcations and chaos in modal interactions of an imperfect circular plate with one-to-one internal resonance have been investigated. The case of primary resonance, in which an excitation frequency is near natural frequencies, is considered. The damping force is not included in the analysis. The method of multiple scales is used to obtain an autonomous system from a non-autonomous system of ordinary differential Equations governing non-linear oscillations of an imperfect circular plate.

The Melnikov method for heteroclinic orbits of the autonomous system is used to obtain the criteria for chaotic motion. It is shown that the existence of heteroclinic orbits in the unperturbed system implies chaos arising from breaking of heteroclinic orbits under perturbation. The validity of the result is checked numerically. It is also observed numerically that chaos can appear due to breaking of invariant tori under perturbation as well as the breaking of heteroclinic orbits.

## Appendix A: Parametrization of heteroclinic orbits

### A.1. On the orbit *A*

Phase portraits of flow (14) for negative $\beta$ in ($P_1$, $Q_1$) plane is shown in Fig. 3 (II). Equations describing

heteroclinic orbits could be simply obtained from Equation $H_0(P_1, Q_1) = H_0(P_1^*, Q_1^*)$, where $(P_1^*, Q_1^*)$ are coordinates of saddle points (15b) which gives:

$$P_1[\beta + (1 + \cos 2Q_1)(P_{20} - P_1)] = 0,$$

with solutions

$$P_1 = \frac{1}{2}\beta \sec^2 Q_1 + P_{20} \tag{A.1a}$$

$$P_1 = 0. \tag{A.1b}$$

First of the above equations corresponds to the orbit $A$, the second to orbits $A'$ and $A''$. Now we are able to obtain explicit time solution of system (13) on heteroclinic orbits.

Substitution (A.1a) into (14b) gives us Equation for $Q_1$

$$Q_1'(t) = -\beta - 2P_{20}\cos^2 Q_1(t).$$

In order to get the expression for orbit $A$ we set the initial condition $Q_1(0) = 0$ and obtain solution

$$Q_1^A(t) = -\arctan[\tan\ p\tilde{Q}_1\ \tanh(e_A t)], \tag{A.2}$$

where

$$e_A = P_{20}\sin(2\ \tilde{Q}_1). \tag{A.3}$$

Now using (A.1a) we can get expression for $P_1(t)$:

$$P_1^A(t) = \frac{P_{20}\sin^2\ \tilde{Q}_1}{\cosh^2(e_A t)}. \tag{A.4}$$

Finally from (13d), (A.2) and (A.4) we get Equation on $Q_2$:

$$Q_2' = -\beta - \sigma - 3P_{20} + \frac{P_{20}\sin^2(2\ \tilde{Q}_1)}{\cos(2\ \tilde{Q}_1) + \cosh(2e_A t)},$$

which could be integrated to give

$$Q_2^A(t) = -\omega_R t - \arctan[\cot\ \tilde{Q}_1\coth(e_A t)] + Q_{20}. \tag{A.5}$$

Here $Q_{20}$ is integration constant and

$$\omega_R = \beta + \sigma + 3P_{20}. \tag{A.6}$$

A.2 On the orbit $A'$ and $A''$

By the same procedure, using Equation (A.1b) we obtain explicit time parametrization of orbits $A'$ and $A''$:

$$P_1^{A'}(t) = 0 \tag{A.7}$$

$$Q_1^{A'}(t) = \arctan[\tan\ \tilde{Q}_1\tanh(e_A t)] \tag{A.8}$$

$$Q_2^{A'}(t) = -\omega_R t + Q_{20} \tag{A.9}$$

$$P_1^{A''}(t) = 0 \tag{A.10}$$

$$Q_1^{A''}(t) = -\arctan\left[\tan\ \tilde{Q}_1\tanh(e_A t)\right] \tag{A.11}$$

$$Q_2^{A''}(t) = -\omega_R t + Q_{20} \tag{A.12}$$

A.3 On the orbit $B$, $B'$ and $B''$

For positive $\beta$ flow (14) in $(P_1, Q_1)$ plane has phase portrait shown in Fig. 3 (III).

The derivation of explicit time parametrization of heteroclinic orbits $B$, $B'$ and $B''$ could be done in the same way as it was shown for case $\beta < 0$.

$$P_1^B(t) = \cos^2\ \tilde{Q}_1 P_{20}[1 + \tan^2\ \tilde{Q}_1\tanh^2(e_A t)] \tag{A.13}$$

$$Q_1^B(t) = \arctan[\tan\ \tilde{Q}_1\tanh(e_A t)] \tag{A.14}$$

$$Q_2^B(t) = (\beta - \omega_R)t + Q_{20} \tag{A.15}$$

$$P_1^{B'}(t) = P_{20} \tag{A.16}$$

$$Q_1^{B'}(t) = -\arctan[\tan\ \tilde{Q}_1\tanh(e_A t)] \tag{A.17}$$

$$Q_2^{B'}(t) = -\arctan[\cot\ \tilde{Q}_1\coth(e_A t)] + (\beta - \omega_R)t + Q_{20} \tag{A.18}$$

$$P_1^{B''}(t) = P_{20} \tag{A.19}$$

$$Q_1^{B''}(t) = -\arctan\left[\frac{\tan\ \tilde{Q}_1}{\tanh(e_A t)}\right] \tag{A.20}$$

$$Q_2^{B''}(t) = -\arctan[\cot\ \tilde{Q}_1\tanh(e_A t)] + (\beta - \omega_R)t + Q_{20}. \tag{A.21}$$

## Appendix B: Calculation of the Melnikov integral for the orbit A

We give the procedure of computation of integrals in Equation (17) for the heteroclinic orbit $A$.

(i) The first integral $I_1$:
Substitution of explicit time dependencies (A.2), (A.4) and (A.5) gives

$$\begin{aligned} I_1 &= \int_{-\infty}^{\infty} \sqrt{P_1}\cos(Q_1+\tilde{Q}_2)\,dt \\ &= \sqrt{P_{20}}\sin\tilde{Q}_1 \int_{-\infty}^{\infty} \cos\{\arctan[\cot\tilde{Q}_1\coth(e_A t)] \\ &\quad + \arctan[\tan\tilde{Q}_1\tanh(e_A t)] \\ &\quad + \omega_R t\}/\cosh(e_A t)\,dt. \end{aligned}$$

By use of trigonometric relation

$$\arctan x + \arctan\frac{1}{x} = \frac{\pi}{2}\operatorname{sign} x$$

integral $I_1$ may be simplified:

$$\begin{aligned} I_1 = \sqrt{P_{20}}\sin\tilde{Q}_1 \Bigg[ &\int_{-\infty}^{0} \frac{\sin(\omega_R t)}{\cosh(e_A t)}dt \\ &- \int_{0}^{\infty} \frac{\sin(\omega_R t)}{\cosh(e_A t)}dt \Bigg] \end{aligned}$$

and solved in terms of digamma functions $\psi(x) = \Gamma'(x)/\Gamma(x)$:

$$I_1 = -\frac{\sqrt{P_{20}}\sin\tilde{Q}_1}{2e_A}\Psi_1\left(\frac{\omega_R}{4e_A}\right),$$

where $\Gamma(x)$ is the gamma function and

$$\begin{aligned} \Psi_1(x) = i\Bigg[ &\psi\left(\frac{1}{4} - i\,x\right) - \psi\left(\frac{1}{4} + i\,x\right) \\ &+ \psi\left(\frac{3}{4} + i\,x\right) - \psi\left(\frac{3}{4} - i\,x\right)\Bigg]. \end{aligned}$$

We should note that $\Psi_1$ is a real-valued function of a real argument.

(ii) The second integral $I_2$:

$$\begin{aligned} I_2 = &\int_{-\infty}^{\infty} \sqrt{P_2 - P_1}\sin\tilde{Q}_2\,dt \\ &-\sqrt{P_{20}}\int_{-\infty}^{\infty}\sqrt{1 - \frac{\sin^2\tilde{Q}_1}{\cosh^2(e_A t)}} \\ &\times \sin\{\arctan[\cot\tilde{Q}_1\coth(e_A t)] - \omega_A t\}\,dt = 0. \end{aligned}$$

We could make the integral vanish by choosing $T_l^s = T_l^u$ for all $l$ since the integrand in the last expression is odd function.

(iii) The third integral $I_3$:
Arguments for the third integral are the same as for the second integral:

$$\begin{aligned} I_3 &= \int_{-\infty}^{\infty} \sqrt{P_1}\sin(Q_1+\tilde{Q}_2)\,dt \\ &= \sqrt{P_{20}}\int_{-\infty}^{\infty} \frac{\sin\tilde{Q}_1}{\cosh(e_A t)} \\ &\quad \times \sin\{-\arctan[\tan\tilde{Q}_1\tanh(e_A t)] \\ &\quad + \arctan[\cot\tilde{Q}_1\coth(e_A t)] - \omega_A t\}\,dt = 0. \end{aligned}$$

(iv) The fourth integral $I_4$:

$$\begin{aligned} I_4 &= \int_{-\infty}^{\infty} \sqrt{P_2 - P_1}\cos\tilde{Q}_2\,dt \\ &= -\sqrt{P_{20}}\int_{-\infty}^{\infty} R(t)\,dt, \end{aligned}$$

where

$$\begin{aligned} R(t) = &\sqrt{1 - \frac{\sin^2\tilde{Q}_1}{\cosh^2(e_A t)}} \\ &\times \cos\{\arctan[\cot\tilde{Q}_1\coth(e_A t)] - \omega_A t\}. \end{aligned}$$

We use the method adapted by Feng and Sethna [13] to solve this integral. Typical behavior of integrand $R(t)$ is shown in Fig. 12. For $t \to \pm\infty$ it behaves as a harmonic function:

$$R(t) \to \sqrt{P_{20}}\sin(\tilde{Q}_1 \mp \omega_R t).$$

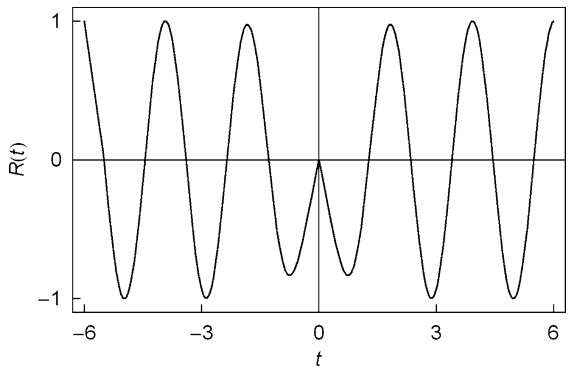


**Fig. 12** Behavior of integrand $R(t)$

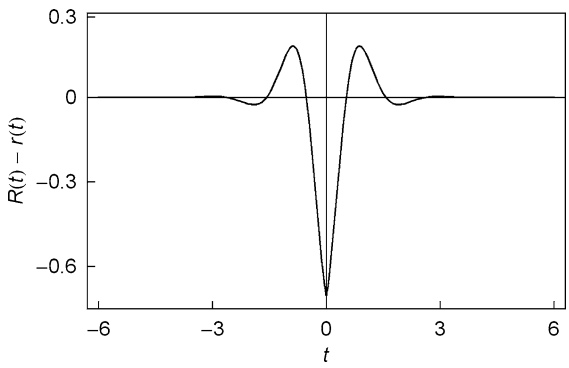


**Fig. 13** Behavior of function $R(t) - r(t)$.

We may rewrite $R(t)$ as

$$R(t) = [R(t) - r(t)] + r(t),$$

where

$$r(t) = \begin{cases} \sqrt{P_{20}}\sin(\tilde{Q}_1 + \omega_R t), & t \le 0 \\ \sqrt{P_{20}}\sin(\tilde{Q}_1 - \omega_R t), & t > 0. \end{cases}$$

Figure 13 shows the typical graph of $R(t) - r(t)$. Integral

$$\int_{-\infty}^{\infty} [R(t) - r(t)]\, dt$$

could be reduced to form

$$2\sin\tilde{Q}_1 \int_{-\infty}^{\infty} \cos(\omega_R t)\,(1 - \tanh(e_A t))\, dt$$

and evaluated in terms of digamma functions as follows:

$$\int_{-\infty}^{\infty} [R(t) - r(t)]\, dt = \frac{\sin\tilde{Q}_1}{2e_A}\Psi_2\left(\frac{\omega_R}{4e_A}\right),$$

where

$$\Psi_2(x) = \psi\left(\frac{1}{2} + ix\right) + \psi\left(\frac{1}{2} - ix\right) - \psi(ix) - \psi(-ix).$$

Function $\Psi_2$ is also a real-valued function of a real argument. Furthermore, we can make the integral $\int_{-T_l^u}^{T_l^s} r(t)\, dt$ vanish by choosing time sequences $T_l^u$ and $T_l^s$ as follows:

$$T_l^u = \frac{\tilde{Q}_1 + l\pi}{\omega_R}, \quad T_l^s = \frac{\tilde{Q}_1 - l\pi}{\omega_R}.$$

Finally we get

$$I_4 = -\sqrt{P_{20}}\left\{\int_{-\infty}^{\infty} [R(t) - r(t)]\, dt + \int_{-\infty}^{\infty} r(t)\, dt\right\} = -\frac{\sqrt{P_{20}}\sin\tilde{Q}_1}{2e_A}\Psi_2\left(\frac{\omega_R}{4e_A}\right).$$

For heteroclinic orbits $A', A'', B, B''$ and $B''$ procedure of calculation of integrals in Equation (17) is similar.

**Acknowledgements** This work was supported by the Yeungnam University research grants in 2003.

## References

1. Tobias, S.A.: Free undamped non-linear vibrations of imperfect circular discs. Proc. Inst. Mech. Eng. **171**, 691–703 (1957)
2. Williams, C.J.H., Tobias, S.A.: Forced undamped non-linear vibrations of imperfect circular discs. Int. J. Mech. Eng. Sci. **5**, 325–335 (1963)
3. Sridhar, S., Mook, D.T., Nayfeh, A.H.: Nonlinear resonances in forced responses of plates, Part I: symmetric responses of circular plates. J. Sound Vib. **41**, 359–373 (1975)
4. Hadian, J., Nayfeh, A.H.: Modal interactions in circular plates. J. Sound Vib. **142**, 279–292 (1990)
5. Lee, W.K., Kim, C.H.: Combination resonances of a circular plate with three-mode interaction. ASME J. Appl. Mech. **62**, 1015–1022 (1995)

6. Sridhar, S., Mook, D.T., Nayfeh, A.H.: Nonlinear resonances in forced responses of plates. Part II: asymmetric responses of circular plates. J. Sound Vib. **59**, 159–170 (1978)
7. Nayfeh, T.A., Vakakis, A.F.: Subharmonic traveling waves in a geometrically non-linear circular plate. Int. J. Non-Linear Mech. **29**(2), 233–245 (1994)
8. Yeo, M.H., Lee, W.K.: Corrected solvability conditions for non-linear asymmetric vibrations of a circular plate. J. Sound Vib. **257**, 653–665 (2002)
9. Lee, W.K., Yeo, M.H.: Nonlinear interactions in asymmetric vibrations of a circular plate. J. Sound Vib. **263**, 1017–1030 (2003)
10. Lee, W.K., Yeo, M.H., Samoilenko, S.B.: The effect of the number of the nodal diameters on non-linear interactions in two asymmetric vibration modes of a circular plate. J. Sound Vib. **268**, 1013–1023 (2003)
11. Touzé, C., Thomas, O., Chaigne, A.: Asymmetric non-linear forced vibrations of free-edge circular plates, Part I: theory. J. Sound Vib. **258**(4), 649–676 (2002)
12. Thomas, O., Touzé, C., Chaigne, A.: Asymmetric non-linear forced vibrations of free-edge circular plates, Part II: experiments. J. Sound Vib. **265**, 1075–1101 (2003)
13. Feng, Z.C., Sethna, P.R.: Global bifurcation and chaos in parametrically forced systems with one-one resonance. Dyn. Stab. Syst. **5**, 201–225 (1990)
14. Kovačič, G., Wiggins, S.: Orbits homoclinic to resonances, with an application to chaos in a model of a forced and damped sine-Gordon Equation. Phys. D **57**, 185–225 (1992)
15. Raman, A., Mote, C.D.: Effects of imperfection on the non-linear oscillations of circular plates spinning near critical speed. Int. J. Non-Linear Mech. **36**, 261–289 (2001)
16. Yeo, M.H., Lee, W.K.: Evidences of global bifurcations of an imperfect circular plate. J. Sound Vib. **293**, 138–155 (2006)
17. Guckenheimer, J., Holmes, P.: Nonlinear Oscillations, Dynamical Systems and Bifuractions of Vector Fields, Springer-Verlag, NY (1983)
18. Wiggins, S.: Global Bifurcations and Chaos. Springer-Verlag, NY (1988)
19. Efstathiades, G.J.: A new approach to the large-deflection vibrations of imperfect circular disks using Galerkin's procedure. J. Sound Vib. **16**, 231–253 (1971)
20. Nayfeh, A.H., Mook, D.T.: Nonlinear Oscillations. Willey, NY (1979)
21. Yang, X.L., Sethna, P.R.: Local and global bifurcations in the parametrically excited vibrations of nearly square plate. Int. J. Non-Linear Mech. **26**, 199–220 (1991)
22. Wiggins, S.: Introduction to Applied Nonlinear Dynamical Systems and Chaos. Springer-Verlag, NY (1990)
23. Ott, E.: Chaos in Dynamical Systems. Cambridge University Press, Cambridge (1993)
24. Moser, J.K.: Lectures on Hamilton systems. Mem. Am. Math. Soc. **81**, 1–60 (1968)
25. Arnol'd, V.I.: Small denominators and problems of stability of motion in classical and celestial mechanics. Russ. Math. Surv. **8**(6), 85–191 (1963)
26. Greene, J.M.: A method for determining a stochastic transition. J. Math. Phy. **20**, 1183–201 (1979)
27. MacKay, R.S.: A renormalization approach to invariant circles in area-preserving maps. Phys. D **7**, 283–300 (1983)
28. Escande, D.F., Doveil, F.: Renormalization method for the onset of stochasticity in a Hamiltonian system. Phys. Lett. A **83**(7), 307–310 (1981)
29. Chandre, C., Govin, M., Jauslin, H.R.: Kolmogorov-Arnold-Moser renormalization-group approach to the breakup of invariant tori in Hamiltonian systems. Phy. Rev. E (3) **57**(2, part A), 1536–1543 (1998)